Calculation of Gilbert damping and magnetic moment of inertia using the torque-torque correlation model within an *ab initio* Wannier framework

Robin Bajaj,[1] Seung-Cheol Lee,[2] H. R. Krishnamurthy,[1] Satadeep Bhattacharjee,[2,*] and Manish Jain[1,†]
[1]*Centre for Condensed Matter Theory, Department of Physics, Indian Institute of Science, Bangalore 560012, India*
[2]*Indo-Korea Science and Technology Center, Bangalore 560065, India*

(Received 31 December 2023; revised 14 May 2024; accepted 29 May 2024; published 21 June 2024)

Magnetization dynamics in magnetic materials are well described by the modified semiclassical Landau-Lifshitz-Gilbert equation, which includes the magnetic damping $\hat{\boldsymbol{\alpha}}$ and the magnetic moment of inertia $\hat{\mathbf{I}}$, both usually being tensors, as key parameters. Both parameters are material specific and physically represent the timescales of damping of precession and nutation in magnetization dynamics. $\hat{\boldsymbol{\alpha}}$ and $\hat{\mathbf{I}}$ can be calculated quantum mechanically within the framework of the torque-torque correlation model. The quantities required for the calculation are torque matrix elements, the real and imaginary parts of the Green's function, and its derivatives. Here, we calculate these parameters for the elemental magnets such as Fe, Co, and Ni in an *ab initio* framework using density functional theory and Wannier functions. We also propose a method to calculate the torque matrix elements within the Wannier framework. We demonstrate the effectiveness of the method by comparing it with the experiments and previous *ab initio* and empirical studies and show its potential to improve our understanding of spin dynamics and to facilitate the design of spintronic devices.

DOI: 10.1103/PhysRevB.109.214432

I. INTRODUCTION

In recent years, the study of spin dynamics [1–5] in magnetic materials has garnered significant attention due to its potential applications in spintronic devices and magnetic storage technologies [6–9]. Understanding the behavior of magnetic moments and their interactions with external perturbations is crucial for the development of efficient and reliable spin-based devices. Among the various parameters characterizing this dynamics, Gilbert damping [10] and magnetic moment of inertia play pivotal roles. The fundamental semiclassical equation describing the magnetization dynamics using these two crucial parameters is the Landau-Lifshitz-Gilbert (LLG) equation [11,12], given by

$$\frac{\partial \boldsymbol{M}}{\partial t} = \boldsymbol{M} \times \left(-\gamma \boldsymbol{H} + \frac{\hat{\boldsymbol{\alpha}}}{M} \frac{\partial \boldsymbol{M}}{\partial t} + \frac{\hat{\mathbf{I}}}{M} \frac{\partial^2 \boldsymbol{M}}{\partial t^2} \right), \tag{1}$$

where $\mathbf{M}$ is the magnetization, $\mathbf{H}$ is the effective magnetic field including both external and internal fields, $\hat{\boldsymbol{\alpha}}$ and $\hat{\mathbf{I}}$ are the Gilbert damping and moment of inertia tensors with the tensor components defined as $\alpha^{\mu\nu}$ and $\mathrm{I}^{\mu\nu}$, respectively, and γ is the gyromagnetic ratio.

Gilbert damping $\hat{\boldsymbol{\alpha}}$ is a fundamental parameter that describes the dissipation of energy during the precession of magnetic moments in response to the external magnetic field. Accurate determination of Gilbert damping is essential for predicting the dynamic behavior of magnetic materials and optimizing their performance in spintronic devices. On the other hand, the magnetic moment of inertia $\hat{\mathbf{I}}$ represents the resistance of a magnetic moment to changes in its orientation. It governs the response time of magnetic moments to external stimuli and influences their ability to store and transfer information. The moment of inertia [13] is the magnetic equivalent of the inertia in classical mechanics [14,15] and acts as the magnetic inertial mass in the LLG equation.

Experimental investigations of Gilbert damping [16–23] and moment of inertia involve various techniques, such as ferromagnetic resonance (FMR) spectroscopy [24,25], spin-torque ferromagnetic resonance (ST-FMR), and time-resolved magneto-optical Kerr effect (TR-MOKE) [26,27]. Interpreting the results obtained from these techniques in terms of the LLG equation provide insights into the dynamical behavior of magnetic materials and can be used to extract the damping and moment of inertia parameters. In order to explain the experimental observations in terms of more microscopic theoretical description, various studies [28–34] based on linear response theory and Kambersky theory have been carried out.

Linear response theory based studies of Gilbert damping and moment of inertia involve perturbing the system and calculating the response of the magnetization to the perturbation. By analyzing the response, one can extract the damping parameter. *Ab initio* calculations based on linear response theory [33] can provide valuable insights into the microscopic mechanisms responsible for the damping process. While formal expression for the moment of inertia in terms of Green's functions has been derived within the linear response framework [11], to the best of our knowledge, there has not been any first-principles electronic-structure-based calculation for the moment of inertia within this formalism.

Kambersky's theory [35–37] describes the damping phenomena using a breathing Fermi surface [38] and torque-torque correlation model [39], wherein the spin-orbit coupling acts as the perturbation and determines the change

*Contact author: s.bhattacharjee@ikst.res.in
†Contact author: mjain@iisc.ac.in

in the nonequilibrium population of electronic states with the change in the magnetic moment direction. Gilmore *et al.* [32,34] have reported the damping for ferromagnets like Fe, Co, and Ni using Kambersky's theory in the linear augmented plane-wave method [40].

The damping and magnetic inertia have been derived within the torque-torque correlation model by expanding the effective dissipation field in the first and second time derivatives of magnetization [29–31]. In this work, the damping and inertia were calculated using the tight-binding model. The parameters are obtained by fitting the electronic band structures to those obtained by fully relativistic multiple scattering Korringa-Kohn-Rostoker (KKR) method using a genetic algorithm [41]. However, there has not been any full *ab intio* implementation using density functional theory (DFT) and Wannier functions to study these magnetic parameters.

The expressions for the damping and inertia involve integration over crystal momentum $\boldsymbol{k}$ in the first Brillouin zone. Accurate evaluation of the integrals involved requires a dense $\boldsymbol{k}$-point mesh of the order of 10^6–10^8 points for obtaining converged values. Calculating these quantities using full *ab initio* DFT is hence time consuming. To overcome this problem, here we propose an alternative. To begin with, the first-principles calculations are done on a coarse $\boldsymbol{k}$ mesh instead of dense $\boldsymbol{k}$ mesh. We then utilize the maximally localized Wannier functions (MLWFs) [42] for obtaining the interpolated integrands required for the denser $\boldsymbol{k}$ meshes. In this method, the gauge freedom of Bloch wave functions is utilized to transform them into a basis of smooth, highly localized Wannier wave functions. The required real-space quantities like the Hamiltonian and torque matrix elements are calculated in the Wannier basis using Fourier transforms. The integrands of integrals can then be interpolated on the fine $\boldsymbol{k}$ mesh by an inverse Fourier transform of the maximally localized quantities, thereby enabling the accurate calculations of the damping and inertia.

The rest of this paper is organized as follows: In Sec. II, we introduce the expressions for the damping and the inertia. We describe the formalism to calculate the two key quantities required, namely, the Green's function and the torque matrix elements, using the Wannier interpolation. In Sec. III, we describe the computational details and workflow. In Sec. IV, we discuss the results for ferromagnets like Fe, Co, and Ni, and discuss the agreement with the experimental values and the previous studies. In Sec. V, we conclude with a short summary.

II. THEORETICAL FORMALISM

First, we describe the expressions for Gilbert damping and moment of inertia within the torque-torque correlation model. Then, we provide a brief description of the MLWFs and the corresponding Wannier formalism for the calculation of torque matrix elements and the Green's function.

A. Gilbert damping and moment of inertia within the torque-torque correlation model

If we consider the case when there is no external magnetic field, the electronic structure of the system can be described by the Hamiltonian

$$\mathcal{H} = \mathcal{H}_0 + \mathcal{H}_{\rm exc} + \mathcal{H}_{\rm SO} = \mathcal{H}_{\rm SP} + \mathcal{H}_{\rm SO}. \tag{2}$$

The paramagnetic band structure is described by $\mathcal{H}_0$ and $\mathcal{H}_{\rm exc}$ describes the effective local electron-electron interaction, treated within a spin-polarized (SP) local Kohn-Sham exchange-correlation (exc) functional approach, which gives rise to the ferromagnetism. $\mathcal{H}_{\rm SO}$ is the spin-orbit Hamiltonian. As we are dealing with ferromagnetic materials only, we can club the first two terms as $\mathcal{H}_{\rm SP} = \mathcal{H}_0 + \mathcal{H}_{\rm exc}$. During magnetization dynamics, (when the magnetization precesses), only the spin-orbit energy of a Bloch state $|\psi_{n\boldsymbol{k}}\rangle$ is effected, where n is the band index of the state. The magnetization precesses around an effective field $\mathbf{H}_{\rm eff} = \mathbf{H}_{\rm int} + \mathbf{H}_{\rm damp} + \mathbf{H}_{\rm I}$, where $\mathbf{H}_{\rm int}$ is the internal field due to the magnetic anisotropy and exchange energies, $\mathbf{H}_{\rm damp}$ is the damping field, and $\mathbf{H}_{\rm I}$ is the inertial field, respectively. From Eq. (1), we can see that the damping field $\mathbf{H}_{\rm damp} = \frac{\hat{\boldsymbol{\alpha}}}{M\gamma}\frac{\partial \boldsymbol{M}}{\partial t}$, while $\mathbf{H}_{\rm I} = \frac{\hat{\mathbf{I}}}{M\gamma}\frac{\partial^2 \boldsymbol{M}}{\partial t^2}$. Equating these damping and inertial fields to the effective field corresponding to the change in band energies as magnetization precesses, we obtain the mathematical description of the Gilbert damping and inertia. It was proposed by Kambersky [39] that the change of the band energies $\frac{\partial \varepsilon_{n\boldsymbol{k}}}{\partial \theta^\mu}$ ($\theta = \theta\hat{n}$ defines the vector for the rotation) can be related to the torque operator (or matrix depending on how the Hamiltonian is being viewed) $\Gamma^\mu = [\sigma^\mu, \mathcal{H}_{\rm SO}]$, where σ^μ are the Pauli matrices. Eventually, within the so-called torque-torque correlation model, the Gilbert damping tensor can be expressed as follows:

$$\alpha^{\mu\nu} = \frac{g}{M_s\pi}\iint\left(-\frac{df(\epsilon)}{d\epsilon}\right)\mathrm{Tr}[\Gamma^\mu(\mathrm{Im}G)(\Gamma^\nu)^\dagger(\mathrm{Im}G)] \times \frac{d^3\boldsymbol{k}}{(2\pi)^3}d\epsilon. \tag{3}$$

Recently, Thonig *et al.* [30] have extended such an approach to the case of moment of inertia also, where they deduced the moment of inertia tensor components to be

$$\mathrm{I}^{\nu\mu} = \frac{g\hbar}{M_s\pi}\iint f(\epsilon)\mathrm{Tr}\Big[\Gamma^\nu(\mathrm{Im}G)(\Gamma^\mu)^\dagger\frac{\partial^2}{\partial\epsilon^2}(\mathrm{Re}G) + \Gamma^\nu\frac{\partial^2}{\partial\epsilon^2}(\mathrm{Re}G)(\Gamma^\mu)^\dagger(\mathrm{Im}G)\Big]\frac{d^3\boldsymbol{k}}{(2\pi)^3}d\epsilon. \tag{4}$$

Here the trace, denoted by Tr, goes over band indices, $f(\epsilon)$ is the Fermi function, (ReG) and (ImG) are the real and imaginary parts of Green's function $G = (\epsilon + \iota\eta - \mathcal{H})^{-1}$ with η as a broadening parameter, M_s is the saturation magnetization in units of the Bohr magneton, $\Gamma^\mu = [\sigma^\mu, \mathcal{H}_{\rm SO}]$ is the μth component of the torque operator or matrix, $\mu = x, y, z$. α is a dimensionless parameter, and I has units of time, usually of the order of femtoseconds.

To obtain the Gilbert damping and moment of inertia tensors from the above two $\boldsymbol{k}$ integrals calculated as sums over discrete $\boldsymbol{k}$ meshes, we need a large number of $\boldsymbol{k}$ points: around 10^6 for ensuring the convergence of α, and more than 10^7 for converging I. The need for an ample $\boldsymbol{k}$-point sampling in the first Brillouin zone (BZ) is caused by the narrowness of Green's function peaks in the vicinity of its poles, for the case of small broadening value η. For I, the required number

of $\boldsymbol{k}$ points is larger in comparison to the case of α because $\partial^2 \mathrm{Re}G/\partial\epsilon^2$ is composed of cubic terms:

$$\frac{\partial^2 \mathrm{Re}G}{\partial\epsilon^2} = 2[(\mathrm{Re}G)^3 - \mathrm{Re}G(\mathrm{Im}G)^2 - \mathrm{Im}G\,\mathrm{Re}G\,\mathrm{Im}G - (\mathrm{Im}G)^2\mathrm{Re}G]. \quad (5)$$

We note that to carry out energy integration in α it is sufficient to consider a limited number of energy points within a narrow range ($\sim k_B T$) around the Fermi level. This is mainly due to the exponential decay of the derivative of the Fermi function away from the Fermi level. However, the integral for I involves the Fermi function itself and not its derivative. Consequently, while the Gilbert damping is associated with the Fermi surface, the moment of inertia is associated with the entire Fermi sea. Therefore, in order to adequately capture both aspects, it is necessary to include energy points between the bottom of the valence band and the Fermi level.

B. Wannier interpolation

1. Maximally localized Wannier functions (MLWFs)

The real-space Wannier functions are written as the Fourier transform of Bloch wave functions

$$|w_{n\boldsymbol{R}}\rangle = \frac{v_0}{(2\pi)^3}\int_{\mathrm{BZ}} d\boldsymbol{k}\, e^{-\iota\boldsymbol{k}\cdot\boldsymbol{R}}|\psi_{n\boldsymbol{k}}\rangle, \quad (6)$$

where $|\psi_{n\boldsymbol{k}}\rangle$ are the Bloch wave functions obtained by the diagonalization of the Hamiltonian at each $\boldsymbol{k}$ point using plane-wave density functional theory (DFT) calculations. v_0 is the volume of the unit cell in the real space.

In general, the Wannier functions obtained by Eq. (6) are not localized. Usually, the Fourier transforms of smooth functions result in localized functions. But there exists a phase arbitrariness of $e^{\iota\phi_{n\boldsymbol{k}}}$ in the Bloch functions because of independent diagonalization at each $\boldsymbol{k}$, which messes up the localization of the Wannier functions in real space.

To mitigate this problem, we use the Marzari-Vanderbilt (MV) localization procedure [42–44] to construct the MLWFs, which are given by

$$|w_{n\boldsymbol{R}}\rangle = \frac{1}{N}\sum_{\boldsymbol{q}}\sum_{m=1}^{\mathcal{N}_{\boldsymbol{q}}} e^{-\iota\boldsymbol{q}\cdot\boldsymbol{R}}\mathcal{U}^{\boldsymbol{q}}_{mn}|\psi_{m\boldsymbol{q}}\rangle, \quad (7)$$

where $\mathcal{U}^{\boldsymbol{q}}_{mn}$ is a $(\mathcal{N}_{\boldsymbol{q}} \times \mathcal{N}_w)$-dimensional matrix chosen by Wannierization procedure. $\mathcal{N}_w$ are the number of target Wannier functions, and $\mathcal{N}_{\boldsymbol{q}}$ are the original Bloch states at each $\boldsymbol{q}$ on the coarse mesh, from which $\mathcal{N}_w$ smooth Bloch states on the fine $\boldsymbol{k}$ mesh are extracted requiring $\mathcal{N}_{\boldsymbol{q}} \geqslant \mathcal{N}_w$ for all $\boldsymbol{q}$, N is the number of uniformly distributed $\boldsymbol{q}$ points in the BZ. The interpolated wave functions on a dense $\boldsymbol{k}$ mesh, therefore, are given via inverse Fourier transform or by summation over $\boldsymbol{R}$ with a cutoff (see Fig. 1) as

$$|\psi^{w}_{n\boldsymbol{k}}\rangle = \sum_{\boldsymbol{R}} e^{\iota\boldsymbol{k}\cdot\boldsymbol{R}}|w_{n\boldsymbol{R}}\rangle. \quad (8)$$

Throughout the paper, we use $\boldsymbol{q}$ and $\boldsymbol{k}$ for coarse and fine meshes in the BZ, respectively. Note that unlike $|\psi_{m\boldsymbol{q}}\rangle$ in Eq. (7), the interpolated wave functions in Eq. (8) are no longer eigenfunctions of the Hamiltonian. Therefore, we used superscript w to represent the interpolated wave functions as $|\psi^{w}_{n\boldsymbol{k}}\rangle$.

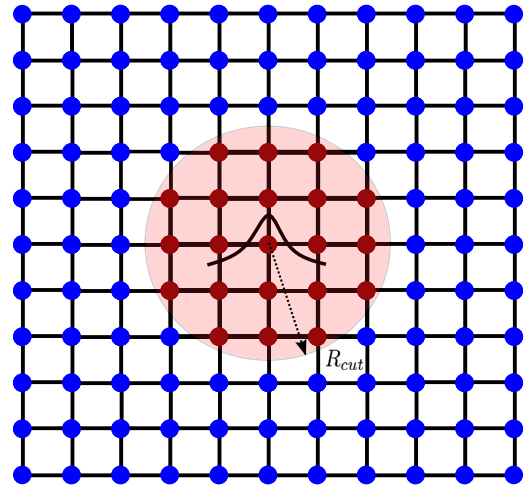

FIG. 1. The figure shows the schematic of the localization of the Wannier functions on a **R** grid. The matrix elements of the quantities like Hamiltonian on the **R** grid are exponentially decaying. Therefore, they can be set to zero for most points on the **R** grid (shown in blue). We can hence do the summation until a cutoff R_{cut} (shown in red) to interpolate the quantities on a fine $\boldsymbol{k}$ grid.

2. Torque matrix elements and Green's functions

As described in the expressions of $\alpha^{\mu\nu}$ and $\mathrm{I}^{\nu\mu}$ in Eqs. (3) and (4), the μth component of the torque matrix is given by the commutator of μth component of Pauli matrices and spin-orbit coupling matrix, i.e., $\Gamma^{\mu} = [\sigma^{\mu}, \mathcal{H}_{\mathrm{SO}}]$. Physically, we define the spin-orbit coupling (SOC) and spin-orbit torque (SOT) as the dot and cross products of orbital angular momentum and spin angular momentum operator, respectively, such that $\mathcal{H}_{\mathrm{SO}} = \xi\boldsymbol{\ell}\cdot\boldsymbol{\sigma}$ where ξ is the coupling amplitude. Using this definition of $\mathcal{H}_{\mathrm{SO}}$, one can show easily that $-\iota[\boldsymbol{\sigma}, \mathcal{H}_{\mathrm{SO}}] = 2\xi\boldsymbol{\ell}\times\boldsymbol{\sigma}$ which represents the torque.

There have been several studies on how to calculate the spin-orbit coupling using the *ab initio* numerical approach. Shubhayan *et al.* [45] describe the method to obtain SOC matrix elements in the Wannier basis calculated without SO interaction, using an approximation of weak SOC in the organic semiconductors considered in their work. Their method involves DFT in the atomic orbital basis, wherein the SOC in the Bloch basis can be related to the SOC in the atomic basis. Then, by the basis transformation, they get the SOC in the Wannier basis calculated in the absence of SO interaction. Farzad *et al.* [46] calculate the SOC by extracting the coupling amplitude from the Hamiltonian in the Wannier basis, treating the Wannier functions as atomiclike orbitals.

We present a different approach wherein we can do the DFT calculation in any basis (plane wave or atomic orbital). Unlike the previous approaches, we perform two DFT calculations and two Wannierizations: one is with spin-orbit interaction and finite magnetization (SO) and the other is spin polarized without spin-orbit coupling (SP). The spin-orbit Hamiltonian $\mathcal{H}_{\mathrm{SO}}$ can then be obtained by subtracting the spin-polarized Hamiltonian $\mathcal{H}_{\mathrm{SP}}$ from the full Hamiltonian $\mathcal{H}$

as $\mathcal{H}_{\rm SO} = \mathcal{H} - \mathcal{H}_{\rm SP}$, provided that both Hamiltonians ($\mathcal{H}$ and $\mathcal{H}_{\rm SP}$) are written in the same Wannier basis. However, when one Wannierizes the SO and SP wave functions, one will get two different Wannier bases. As a result, we can not directly subtract the $\mathcal{H}$ and $\mathcal{H}_{\rm SP}$ in these close but different Wannier bases. In order to do the subtraction, we find the transformation between the two Wannier bases, i.e., express one set of Wannier functions in terms of the other. Subsequently, we can express the matrix elements of $\mathcal{H}$ and $\mathcal{H}_{\rm SP}$ in the same basis and hence calculate $\mathcal{H}_{\rm SO}$. In the equations below, the Wannier functions, the Bloch wave functions and the operators defined in the corresponding bases in SP and SO calculations are represented with and without the tilde ($\sim$) symbol, respectively.

The $\mathcal{N}_w$ SO Wannier functions $|w_{n\boldsymbol{R}}\rangle$ are related to SO Bloch wave functions $|\psi_{m\boldsymbol{q}}\rangle$ by

$$|w_{n\boldsymbol{R}}\rangle = \frac{1}{N}\sum_{\boldsymbol{q}}\sum_{m=1}^{\mathcal{N}_{\boldsymbol{q}}} e^{-\iota\boldsymbol{q}\cdot\boldsymbol{R}}\mathcal{U}^{\boldsymbol{q}}_{mn}|\psi_{m\boldsymbol{q}}\rangle, \tag{9}$$

where $\mathcal{U}^{\boldsymbol{q}}_{mn}$ is a $(\mathcal{N}_{\boldsymbol{q}} \times \mathcal{N}_w)$-dimensional matrix. The SO wave functions and Wannier functions are superpositions of up- and down-spin states and can be represented as spinors:

$$|\psi_{n\boldsymbol{q}}\rangle = \begin{bmatrix} |\psi^{\uparrow}_{n\boldsymbol{q}}\rangle \\ |\psi^{\downarrow}_{n\boldsymbol{q}}\rangle \end{bmatrix}, \quad |w_{n\boldsymbol{R}}\rangle = \begin{bmatrix} |w^{\uparrow}_{n\boldsymbol{R}}\rangle \\ |w^{\downarrow}_{n\boldsymbol{R}}\rangle \end{bmatrix}. \tag{10}$$

The $\tilde{\mathcal{N}}^s_w$ SP Wannier functions $|\tilde{w}^s_{n\boldsymbol{R}}\rangle$, are related to the SP Bloch wave functions $|\tilde{\psi}^s_{m\boldsymbol{q}}\rangle$ by

$$\left|\tilde{w}^s_{n\boldsymbol{R}}\right\rangle = \frac{1}{N}\sum_{\boldsymbol{q}}\sum_{m=1}^{\tilde{\mathcal{N}}^s_{\boldsymbol{q}}} e^{-\iota\boldsymbol{q}\cdot\boldsymbol{R}}\tilde{\mathcal{U}}^{\boldsymbol{q}s}_{mn}\left|\tilde{\psi}^s_{m\boldsymbol{q}}\right\rangle, \tag{11}$$

where $s = \uparrow, \downarrow$. $\tilde{\mathcal{U}}^{\boldsymbol{q}s}_{mn}$ is a $(\tilde{\mathcal{N}}^s_{\boldsymbol{q}} \times \tilde{\mathcal{N}}^s_w)$-dimensional matrix. The off-diagonal terms in the spin-polarized Hamiltonian corresponding to opposite spins are zero (because of no SOC). As a result, the SP Bloch wave functions are the eigenstates of the σ_z operator. The SP Bloch wave function in the σ_z basis, $|\tilde{\psi}_{m\boldsymbol{q}}\rangle$, can be written as

$$|\tilde{\psi}_{m\boldsymbol{q}}\rangle = \left\{ \begin{bmatrix} |\tilde{\psi}^{\uparrow}_{m\boldsymbol{q}}\rangle \\ 0 \end{bmatrix} \quad \text{for } m = 1, \ldots, \tilde{\mathcal{N}}^{\uparrow}_{\boldsymbol{q}} \right\} \\ \left\{ \begin{bmatrix} 0 \\ |\tilde{\psi}^{\downarrow}_{m\boldsymbol{q}}\rangle \end{bmatrix} \quad \text{for } m = \tilde{\mathcal{N}}^{\uparrow}_{\boldsymbol{q}} + 1, \ldots, \tilde{\mathcal{N}}^{\uparrow}_{\boldsymbol{q}} + \tilde{\mathcal{N}}^{\downarrow}_{\boldsymbol{q}} \right\}. \tag{12}$$

The corresponding $\tilde{\mathcal{N}}_w$ SP Wannier functions in the σ_z basis, $|\tilde{w}_{n\boldsymbol{R}}\rangle$, with $\tilde{\mathcal{N}}_w = \tilde{\mathcal{N}}^{\uparrow}_w + \tilde{\mathcal{N}}^{\downarrow}_w$, can be written as

$$|\tilde{w}_{n\boldsymbol{R}}\rangle = \frac{1}{N}\sum_{\boldsymbol{q}}\sum_{m=1}^{\tilde{\mathcal{N}}_{\boldsymbol{q}}} e^{-\iota\boldsymbol{q}\cdot\boldsymbol{R}}\tilde{\mathcal{U}}^{\boldsymbol{q}}_{mn}|\tilde{\psi}_{m\boldsymbol{q}}\rangle, \tag{13}$$

where $\tilde{\mathcal{U}}^{\boldsymbol{q}}$ is $(\tilde{\mathcal{N}}_{\boldsymbol{q}} \times \tilde{\mathcal{N}}_w)$-dimensional matrix with $\tilde{\mathcal{N}}_{\boldsymbol{q}} = \tilde{\mathcal{N}}^{\uparrow}_{\boldsymbol{q}} + \tilde{\mathcal{N}}^{\downarrow}_{\boldsymbol{q}}$. $\tilde{\mathcal{U}}^{\boldsymbol{q}}$ can be represented in the σ_z basis as

$$\tilde{\mathcal{U}}^{\boldsymbol{q}} = \begin{bmatrix} \tilde{\mathcal{U}}^{\boldsymbol{q}\uparrow} & 0 \\ 0 & \tilde{\mathcal{U}}^{\boldsymbol{q}\downarrow} \end{bmatrix} \tag{14}$$

and $|\tilde{w}_{n\boldsymbol{R}}\rangle$ can be represented as

$$|\tilde{w}_{n\boldsymbol{R}}\rangle = \left\{ \begin{bmatrix} |\tilde{w}^{\uparrow}_{n\boldsymbol{R}}\rangle \\ 0 \end{bmatrix} \quad \text{for } n = 1, \ldots, \tilde{\mathcal{N}}^{\uparrow}_w \right\} \\ \left\{ \begin{bmatrix} 0 \\ |\tilde{w}^{\downarrow}_{n\boldsymbol{R}}\rangle \end{bmatrix} \quad \text{for } n = \tilde{\mathcal{N}}^{\uparrow}_w + 1, \ldots, \tilde{\mathcal{N}}^{\uparrow}_w + \tilde{\mathcal{N}}^{\downarrow}_w \right\}. \tag{15}$$

We now define the matrix of the transformation between SO and SP Wannier bases as

$$\begin{aligned} T^{\boldsymbol{RR}'}_{mn} &= \langle \tilde{w}_{m\boldsymbol{R}}|w_{n\boldsymbol{R}'}\rangle \\ &= \frac{1}{N^2}\sum_{\boldsymbol{q}\boldsymbol{q}'}\sum_{p,l=1}^{\tilde{\mathcal{N}}_{\boldsymbol{q}},\mathcal{N}_{\boldsymbol{q}'}} e^{\iota(\boldsymbol{q}\cdot\boldsymbol{R}-\boldsymbol{q}'\cdot\boldsymbol{R}')}\tilde{\mathcal{U}}^{\boldsymbol{q}\dagger}_{mp}\langle\tilde{\psi}_{p\boldsymbol{q}}|\psi_{l\boldsymbol{q}'}\rangle\mathcal{U}^{\boldsymbol{q}'}_{ln} \\ &= \frac{1}{N^2}\sum_{\boldsymbol{q}\boldsymbol{q}'} e^{\iota(\boldsymbol{q}\cdot\boldsymbol{R}-\boldsymbol{q}'\cdot\boldsymbol{R}')}[\tilde{\mathcal{U}}^{\boldsymbol{q}\dagger}\mathcal{V}^{\boldsymbol{q}\boldsymbol{q}'}\mathcal{U}^{\boldsymbol{q}'}]_{mn}, \end{aligned} \tag{16}$$

where $\mathcal{V}^{\boldsymbol{q}\boldsymbol{q}'}_{pl} = \langle\tilde{\psi}_{p\boldsymbol{q}}|\psi_{l\boldsymbol{q}'}\rangle$. Equation (16) is the most general expression to get the transformation matrix. We can reduce this quantity to a much simpler one using the orthogonality of wave functions of different $\boldsymbol{q}$. Equation (16) hence becomes

$$\begin{aligned} T^{\boldsymbol{RR}'}_{mn} &= \frac{1}{N^2}\sum_{\boldsymbol{q}} e^{\iota\boldsymbol{q}\cdot(\boldsymbol{R}-\boldsymbol{R}')}[\tilde{\mathcal{U}}^{\boldsymbol{q}\dagger}(N\mathcal{V}^{\boldsymbol{q}})\mathcal{U}^{\boldsymbol{q}}]_{mn} \\ &= \frac{1}{N}\sum_{\boldsymbol{q}} e^{\iota\boldsymbol{q}\cdot(\boldsymbol{R}-\boldsymbol{R}')}[\tilde{\mathcal{U}}^{\boldsymbol{q}\dagger}\mathcal{V}^{\boldsymbol{q}}\mathcal{U}^{\boldsymbol{q}}]_{mn} \end{aligned} \tag{17}$$

where $\mathcal{V}^{\boldsymbol{q}}_{pl} = \langle\tilde{\psi}_{p\boldsymbol{q}}|\psi_{l\boldsymbol{q}}\rangle$. Using this transformation, we write the SP Hamiltonian in SO Wannier bases as

$$\begin{aligned} (\mathcal{H}_{\rm SP})^{\boldsymbol{RR}'}_{mn} &= \langle w_{m\boldsymbol{R}}|\mathcal{H}_{\rm SP}|w_{n\boldsymbol{R}'}\rangle \\ &= \sum_{pl\boldsymbol{R}''\boldsymbol{R}'''}\langle w_{m\boldsymbol{R}}|\tilde{w}_{p\boldsymbol{R}''}\rangle \\ &\quad\times\langle\tilde{w}_{p\boldsymbol{R}''}|\mathcal{H}_{\rm SP}|\tilde{w}_{l\boldsymbol{R}'''}\rangle\langle\tilde{w}_{l\boldsymbol{R}'''}|w_{n\boldsymbol{R}'}\rangle \\ &= \sum_{pl\boldsymbol{R}''\boldsymbol{R}'''}(T^{\dagger})^{\boldsymbol{RR}''}_{mp}(\tilde{\mathcal{H}}_{\rm SP})^{\boldsymbol{R}''\boldsymbol{R}'''}_{pl}T^{\boldsymbol{R}'''\boldsymbol{R}'}_{ln}. \end{aligned} \tag{18}$$

Since Wannier functions are maximally localized and generally atomiclike, the major contribution to the overlap $T^{\boldsymbol{RR}'}_{mn}$ is for $\boldsymbol{R} = \boldsymbol{R}'$. Therefore, we can write $T^{\boldsymbol{RR}}_{mn} = T^{\boldsymbol{0}}_{mn}$. The reason is that it depends on relative $\boldsymbol{R} - \boldsymbol{R}'$, we can just consider overlaps at $\boldsymbol{R} = \boldsymbol{0}$. Equation (18) becomes

$$(\mathcal{H}_{\rm SP})^{\boldsymbol{RR}'}_{mn} = \sum_{pl}(T^{\dagger})^{\boldsymbol{0}}_{mp}(\tilde{\mathcal{H}}_{\rm SP})^{\boldsymbol{RR}'}_{pl}T^{\boldsymbol{0}}_{ln}. \tag{19}$$

Therefore, we write the $\mathcal{H}_{\rm SO}$ in Wannier basis as

$$(\mathcal{H}_{\rm SO})^{\boldsymbol{RR}'}_{mn} = \mathcal{H}^{\boldsymbol{RR}'}_{mn} - (\mathcal{H}_{\rm SP})^{\boldsymbol{RR}'}_{mn}. \tag{20}$$

The torque matrix elements in SO Wannier bases are given by

$$(\Gamma^{\mu})^{\boldsymbol{RR}'}_{mn} = (\sigma^{\mu}\mathcal{H}_{\rm SO})^{\boldsymbol{RR}'}_{mn} - (\mathcal{H}_{\rm SO}\sigma^{\mu})^{\boldsymbol{RR}'}_{mn}. \tag{21}$$

Consider $(\sigma^{\mu}\mathcal{H}_{\rm SO})^{\boldsymbol{RR}'}_{mn}$ and insert the completeness relation of the Wannier functions, and also neglecting SO matrix

elements between the Wannier functions at different sites because of their being atomiclike:

$$(\sigma^\mu \mathcal{H}_{\rm SO})^{\boldsymbol{RR'}}_{mn} = \textstyle\sum_{p\boldsymbol{R''}} (\sigma^\mu)^{\boldsymbol{RR''}}_{mp} (\mathcal{H}_{\rm SO})^{\boldsymbol{R''R'}}_{pn} = (\sigma^\mu)^{\boldsymbol{RR'}}_{mp} (\mathcal{H}_{\rm SO})^{\boldsymbol{0}}_{pn}. \tag{22}$$

$(\sigma^\mu)^{\boldsymbol{RR'}}_{mp}$ is calculated by the Fourier transform of the spin operator written in the Bloch basis, just like the Hamiltonian:

$$(\sigma^\mu)^{\boldsymbol{RR'}}_{mp} = \frac{1}{N} \sum_{\boldsymbol{q}} e^{-\iota \boldsymbol{q}\cdot(\boldsymbol{R'}-\boldsymbol{R})} [\mathcal{U}^{\boldsymbol{q}\dagger} (\sigma^\mu)^{\boldsymbol{q}} \mathcal{U}^{\boldsymbol{q}}]_{mp}. \tag{23}$$

We interpolate the SOT matrix elements on a fine $\boldsymbol{k}$ mesh as follows:

$$(\Gamma^\mu)^{\boldsymbol{k}}_{mn} = \sum_{\boldsymbol{R'}-\boldsymbol{R}} e^{\iota \boldsymbol{k}\cdot(\boldsymbol{R'}-\boldsymbol{R})} (\sigma^\mu)^{\boldsymbol{RR'}}_{mn}. \tag{24}$$

This yields the torque matrix elements in the Wannier basis. In the subsequent expressions, W and H subscripts represent the Wannier and Hamiltonian basis, respectively. In order to rotate to the Hamiltonian basis, which diagonalizes the Hamiltonian interpolated on the fine $\boldsymbol{k}$ mesh using its matrix elements in the Wannier basis,

$$(\mathcal{H}_W)^{\boldsymbol{k}}_{mn} = \sum_{\boldsymbol{R'}-\boldsymbol{R}} e^{\iota \boldsymbol{k}\cdot(\boldsymbol{R'}-\boldsymbol{R})} \mathcal{H}^{\boldsymbol{RR'}}_{mn}, \tag{25}$$

$$(\mathcal{H}_H)^{\boldsymbol{k}}_{mn} = [(U^{\boldsymbol{k}})^\dagger (\mathcal{H}_W)^{\boldsymbol{k}} U^{\boldsymbol{k}}]_{mn}. \tag{26}$$

Here $U^{\boldsymbol{k}}$ (not to be confused with $\mathcal{U}^{\boldsymbol{q}}$) are the matrices with columns as the eigenvectors of $(\mathcal{H}_W)^{\boldsymbol{k}}$, and $(\mathcal{H}_H)^{\boldsymbol{k}}_{mn} = \epsilon_{m\boldsymbol{k}}\delta_{mn}$. We use these matrices to rotate the SOT matrix elements in Eq. (24) to the Hamiltonian basis as

$$\left(\Gamma^\mu_H\right)^{\boldsymbol{k}}_{mn} = \left[(U^{\boldsymbol{k}})^\dagger \left(\Gamma^\mu_W\right)^{\boldsymbol{k}} U^{\boldsymbol{k}}\right]_{mn}. \tag{27}$$

The Green's function at an arbitrary $\boldsymbol{k}$ and ϵ on a fine $\boldsymbol{k}$ mesh in the Hamiltonian basis is given by

$$G^{\boldsymbol{k}}_H(\epsilon + \iota\eta) = [\epsilon + \iota\eta - (\mathcal{H}_H)^{\boldsymbol{k}}]^{-1}, \tag{28}$$

where η is a broadening factor and is caused by electron-phonon coupling and is generally of the order 5–10 meV. $G^{\boldsymbol{k}}_H(\epsilon + \iota\eta)$ is a $(\mathcal{N}\times\mathcal{N})$-dimensional matrix.

Therefore, we can calculate ReG, ImG, and $\partial^2 \mathrm{Re}G/\partial\epsilon^2$ as defined in Eq. (5) and, hence, α and I. The implementation flow chart based on the above-described procedure has been shown in Fig. 2.

There are, however, some limitations of this approach: materials with very large spin-orbit coupling, and antiferromagnets. Our method of calculating the spin-orbit torque matrix elements in Wannier framework is perturbative. Therefore, in the case of significant variation of the Hartree field or exchange energy terms in the strong spin-orbit coupling regime, this method may not estimate correctly the Gilbert damping coefficient. But there is an alternative to effectively suppress those effects on the matrix elements of the Hamiltonian. We know that in the Wannier and atomiclike bases, the spin-orbit coupling and torque matrix elements should be of the form $\mathcal{H}_{\rm SO} = \xi\boldsymbol{\ell}\cdot\boldsymbol{\sigma}$ and $2\xi\boldsymbol{\ell}\times\boldsymbol{\sigma}$, respectively. Therefore, for the strong spin-orbit coupling, we can manually suppress effects of Hartree and exchange terms for all matrix elements where it should vanish. This approach should give the correct estimate of the Gilbert damping and the moment of inertia.

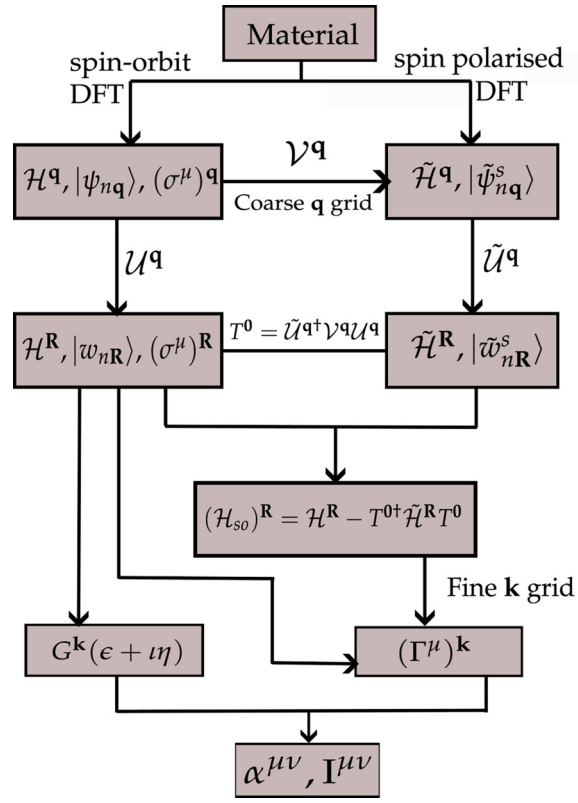

FIG. 2. This figure shows the implementation flow chart of the theoretical formalism described in Sec. II.

In antiferromagnets, the damping tensor is $\alpha_{ss'}$, where s and s' correspond to two sublattices with the opposite orientation of spins [47]. By solving the coupled LLG equations for s and s' in the absence of external magnetic field, one can show that the antiferromagnetic resonance (AFMR) linewidth is composed of two damping components, α_r and $\alpha_{\rm ex}$, which represent the relativistic component arising from spin-orbit coupling and the exchange component arising from spin exchange between the two sublattices, respectively [48]. The expression for α_r is similar to torque-torque correlation, and therefore can be calculated using the described Wannier formalism. But in AFMs, α_r is usually smaller by three orders of magnitude in comparison to $\alpha_{\rm ex}$. In this case, it is important to use the described approach for exchange torque calculations: $-i[\hat{S}^\pm, \hat{H}_{\rm xc}] = \mp iU_h M\hat{S}^\pm$. Here, U_h and M are, respectively, the Stoner-Hubbard parameter and the magnetization, which can be estimated in the Wannier basis for AFMs by fitting it with the Wannier Hamiltonian to get U_h. This method is analogous to estimating the coupling ξ in the spin-orbit part using the Hamiltonian written in the Wannier basis. Therefore, the Wannier-based approach may approximately quantify the damping for AFMs as well.

III. COMPUTATIONAL DETAILS

Plane-wave pseudopotential calculations were carried out for the bulk ferromagnetic transition metals bcc Fe, hcp Co, and fcc Ni using the QUANTUM ESPRESSO package [49,50]. The conventional unit-cell lattice constants (a) used for bcc Fe and fcc Ni were 5.424 and 6.670 bohrs, respectively, and

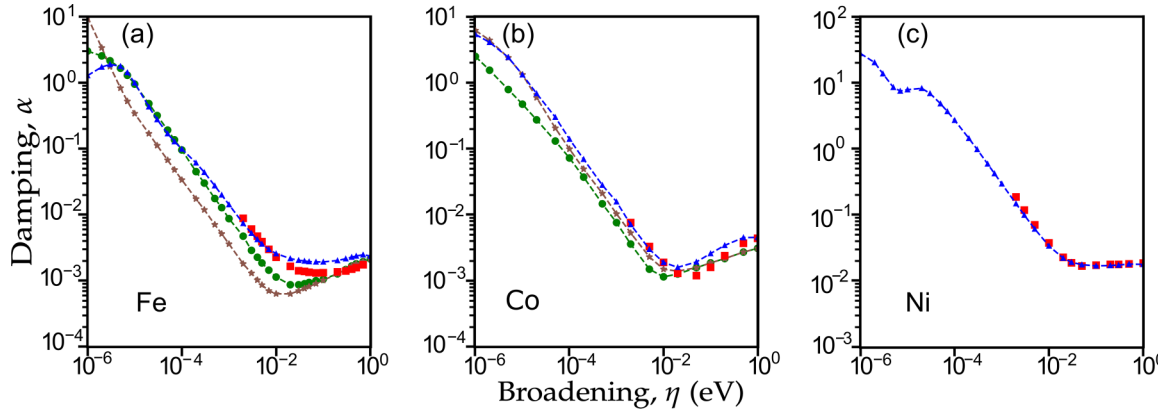

FIG. 3. (a)–(c) Show the plots of α vs η for Fe, Co, and Ni, respectively. Damping constants calculated using the Wannier implementation are shown in blue. Dampings calculated using the tight-binding method based on Lorentzian broadening and Green's function by Thonig *et al.* [29] are shown in brown and green, respectively. Damping coefficients calculated by Gilmore *et al.* [32] using local spin density approximation (LSDA) are shown in red. The dashed curves are guides to the eye.

for hcp Co, $a = 4.738$ bohrs and $c/a = 1.623$ were used. The noncollinear spin-orbit and spin-polarized calculations were performed using fully relativistic norm-conserving pseudopotentials. The kinetic energy cutoff was set to 80 Ry. Exchange-correlation effects were treated within the PBE-GGA approximation. The self-consistent calculations were carried out on a $16 \times 16 \times 16$ Monkhorst-Pack grid using Fermi smearing of 0.02 Ry. Non-self-consistent calculations were carried out using the calculated charge densities on a Γ-centered $10 \times 10 \times 10$ coarse $\boldsymbol{k}$-point grid. For bcc Fe and fcc Ni, 64 bands were calculated, and for hcp Co 96 bands were calculated (because there are two atoms per unit cell for Co). We define a set of 18 trial hybrid orbitals sp^3d^2, d_{xy}, d_{xz}, and d_{yz} for Fe, as well as trial orbitals without any hybridization, also 18 per atom s, p, and d for Co and Ni, to generate 18 maximally localized spinor Wannier functions per atom using the WANNIER90 package [43].

From the WANNIER90 calculations, we get the checkpoint file *.chk*, which contains all the information about the gauge matrices. We use the *.spn* and *.eig* files generated by PW2WANNIER90 to get the spin operator and the Hamiltonian in the Wannier basis. We evaluate the SOT matrix elements in the Wannier basis.

We get α by simply summing up on a fine-$\boldsymbol{k}$ grid the integrand in Eq. (3) with appropriate weights for the $\boldsymbol{k}$ integration, and we use the trapezoidal rule in the range $[-8\delta, 8\delta]$ for energy integration around the Fermi level where δ is the width of the derivative of Fermi function $\sim k_B T$. We consider 34 energy points in this energy range. We perform the calculation for $T = 300$ K.

For the calculation of I, we use a very fine grid of $400 \times 400 \times 400$ $\boldsymbol{k}$ points. For $\eta > 0.1$, we use 320 energy points between valence band minimum (VBM) and Fermi energy. For $0.01 < \eta < 0.1$, we use 3200–6400 energy points for the energy integration.

IV. RESULTS AND DISCUSSION

A. Gilbert damping

In this section, we report the Gilbert damping constants calculated for the bulk iron, cobalt, and nickel. If we choose the z direction to be oriented along the direction of magnetization, the damping tensor is diagonal, resulting in the effective damping constant $\alpha = \alpha^{xx} + \alpha^{yy}$.

In Fig. 3, we report the damping constants calculated by the Wannier implementation as a function of the broadening η known to be caused by electron-phonon scattering and scattering due to impurities. In this study, η was varied in the range 10^{-6}–1 eV for clarifying the contributions of intraband and interband transitions, following the methodology reported in Refs. [29,32]. The upper limit of the range $\eta = 1$ eV was chosen because above this value our model ceases to produce realistic results. The broadening range observed

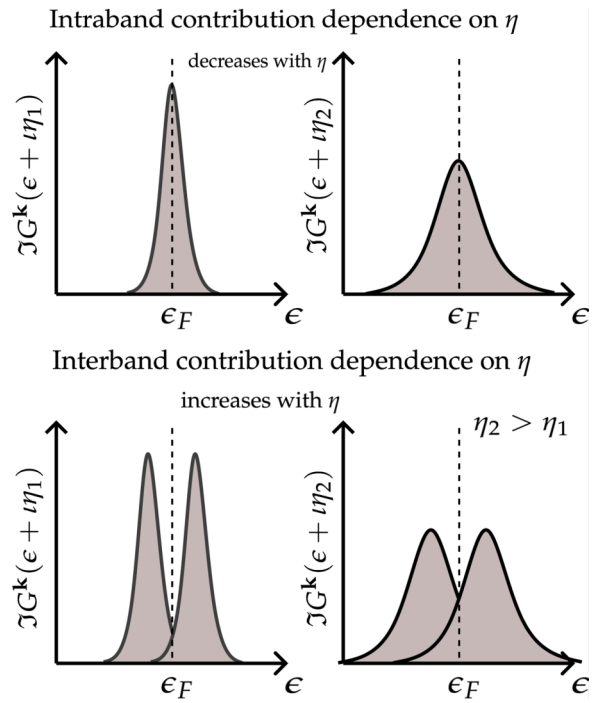

FIG. 4. Schematic diagrams illustrating the influence of the broadening parameter η on the intraband and interband contributions to the damping coefficient α.

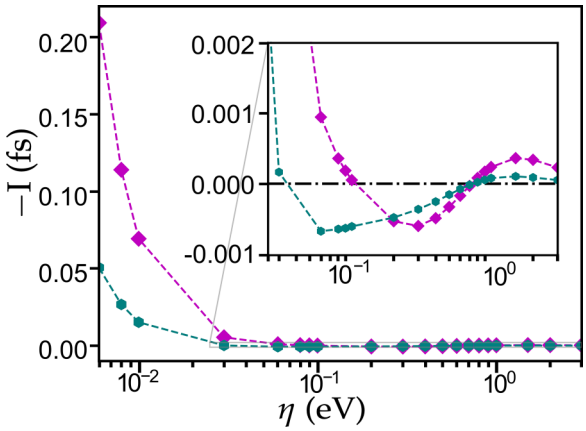

FIG. 5. Plot showing the moment of inertia −I versus broadening η for Fe. The moment of inertia in the range 0.03–3.0 eV is shown as an inset. The values using the Wannier implementation and the tight-binding method [30] are shown in magenta and cyan, respectively.

experimentally is considerably narrower, $\eta \approx 5$–10 meV. Our calculation results agree well with those obtained using local spin density approximation [32,51] and tight-binding parametrization [29].

The expression for Gilbert damping in Eq. (3) is written in terms of the imaginary part of Green's functions. Using the spectral representation of Green's function $A_{nk}(\omega)$, we can rewrite Eq. (3) as

$$\alpha^{\mu\nu} = \frac{g\pi}{M_s} \sum_{nm} \int T^{\mu}_{nm}(\boldsymbol{k}) T^{*\nu}_{nm}(\boldsymbol{k}) S_{nm} d\boldsymbol{k}, \tag{29}$$

where $S_{nm} = \int \eta(\epsilon) A_{nk}(\epsilon) A_{mk}(\epsilon) \mathrm{d}\epsilon$ is the spectral overlap. Although we are working in the basis where the Hamiltonian is diagonal, the nonzero off-diagonal elements in the torque matrix lead to both intraband ($m = n$) and interband ($m \neq n$) contributions. For the sake of simple physical understanding, we consider the contribution of the spectral overlaps at the Fermi level for both intraband and interband transitions in Fig. 4. But in the numerical calculation thermal broadening has also been taken into account. For the smaller η, the contribution of intraband transitions decreases almost linearly with the increase in η because overlapping peaks are of smaller height and larger width as shown in Fig. 4. Above a certain η, the interband transitions become dominant and the contribution due to the overlap of two spectral functions at different band indices m and n becomes more pronounced at the Fermi level. With further increase in η, the interband contribution increases until $\eta \sim 1$ eV. Because of the finite Wannier orbitals basis, we have an accurate description of energy bands only within the approximate range of $(\epsilon_F - 10, \epsilon_F + 5)$ eV for the ferromagnets in consideration.

B. Moment of inertia

Figures 5 and 6 show the moment of inertia for bulk Fe, Co, and Ni. Analogous to the Gilbert damping, the inertia tensor is diagonal, resulting in the effective moment of inertia $\mathrm{I} = \mathrm{I}^{xx} + \mathrm{I}^{yy}$.

The behavior for I vs η is similar to that of the damping, with smaller and larger η trends arising because of intraband and interband contributions, respectively. The overlap term in the moment of inertia is between the $\partial^2 \mathrm{Re}G/\partial\epsilon^2$ and ImG unlike just ImG in the damping. In Ref. [30], the moment of inertia is defined in terms of torque matrix elements and the overlap matrix as

$$\mathrm{I}^{\mu\nu} = -\frac{g\hbar}{M_s} \sum_{nm} \int T^{\mu}_{nm}(\boldsymbol{k}) T^{*\nu}_{nm}(\boldsymbol{k}) V_{nm} d\boldsymbol{k}, \tag{30}$$

where V_{nm} is an overlap function, given by $\int f(\epsilon)[A_{nk}(\epsilon)B_{mk}(\epsilon) + B_{nk}(\epsilon)A_{mk}(\epsilon)]\mathrm{d}\epsilon$ and $B_{mk}(\epsilon)$ is given by $2(\epsilon - \epsilon_{mk})[(\epsilon - \epsilon_{mk})^2 - 3\eta^2]/[(\epsilon - \epsilon_{mk})^2 + \eta^2]^3$. There are other notable features different from the damping. In the limit $\eta \to 0$, the overlap V_{mn} reduces to $2/(\epsilon_{mk} - \epsilon_{nk})^3$. For intraband transitions ($m = n$), this leads to $\mathrm{I} \to -\infty$. In the limit $\eta \to \infty$, $V_{mn} \approx 1/\eta^5$ which leads to $\mathrm{I} \to 0$. The behavior at these two limits is evident from Figs. 5 and 6. The large-τ (small-η) behavior is consistent with the expression $\mathrm{I} = -\alpha.\tau/2\pi$ derived by Fähnle *et al.* [52]. Here τ is the Bloch relaxation lifetime. The behavior of τ as a function of η using the above expression in the low-η limit is shown in Fig. 7. Apart from these limits, the sign change

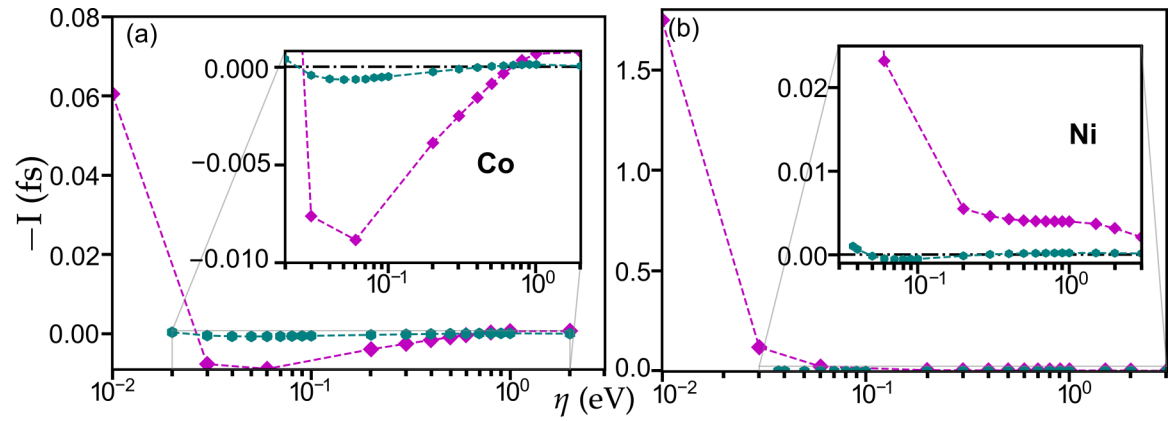

FIG. 6. (a), (b) Show the moment of inertia −I versus broadening η for Co and Ni, respectively. The values using the Wannier implementation and the tight-binding method are shown in magenta and cyan, respectively. Insets: the moment of inertia in the range 0.02–2.0 eV and 0.03–3.0 eV for Co and Ni, respectively.

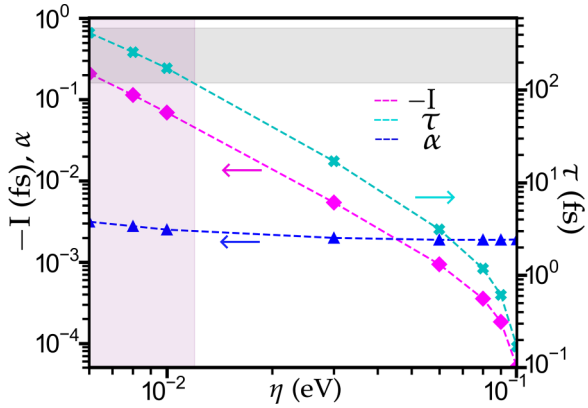

FIG. 7. The damping, magnetic moment of inertia, and relaxation rate for Fe are shown as functions of the broadening η in blue, pink, and cyan, respectively. The gray-shaded region shows the observed experimental relaxation rate τ, ranging from 0.12 to 0.47 ps. The η range of 6–12 meV is highlighted with a purple rectangle (see Table I for the corresponding numerical values for Fe, Co, and Ni). This agrees with the experimental broadening in the range of 5–10 meV, arising from electron-phonon coupling.

has been observed in a certain range of η for Fe and Co. This change in sign can be explained by Eq. (5). In the regime where intraband contributions dominate, at a certain η the negative and positive terms integrated over ϵ and $\boldsymbol{k}$ become the same, leading to zero inertia. Above that η, the contribution due to the negative terms decreases until the interband contribution plays a major role leading to a local maximum in I (a local minimum in $-$I). Interband contribution leads to the sign change from $+$ to $-$ and eventually zero at larger η. This local minimum in $-$I can be seen at the broadening of around 0.3 and 0.06 eV for Fe and Co, respectively [see Figs. 5 and 6(a)].

In the small-η regime, the moment of inertia and the Gilbert damping are related by $\mathrm{I} = -\alpha.\tau/2\pi$, which indicates that damping and the moment of inertia have opposite signs. By analyzing the rate of change of magnetic energy, Ref. [11] shows that Gilbert damping and the moment of inertia have opposite signs when the magnetization dynamics is sufficiently slow (compared to τ).

FMR measurements on $Ni_{79}Fe_{21}$ and Co thin films have experimentally elucidated the origin of the anomalous inertia sign [27]. The third term in Eq. (1), involving second-order time derivative, results in an effective field (H_{eff}) that is quadratic in frequency. One can show that the negative and positive values of the moment of inertia correspond to positive and negative values of H_{eff}, respectively. This directly reflects the stiffening and softening behavior in H_{eff} versus ω at higher frequencies, analogous to the stiffening or softening on force versus displacement at larger displacements. The experimentally observed frequency dependence of resonance fields confirms the stiffening behavior, which indicates the negative values of the moment of inertia. The softening caused by positive values of the moment of inertia is not observed experimentally. This is because the experimentally realized

TABLE I. Theoretically calculated values of $-$I, α, and τ for Fe, Co, and Ni for different values of η.

Material	η (meV)	$-$I (fs)	$\alpha(\times 10^{-3})$	τ (ps)
Fe	6	0.210	3.14	0.42
	8	0.114	2.77	0.26
	10	0.069	2.51	0.17
Co	10	0.061	1.9	0.21
Ni	10	1.747	34.2	0.32

broadening η caused by electron-phonon scattering and scattering from impurities is of the order of 5–10 meV. The values of Bloch relaxation lifetime τ measured at the room temperature with the FMR in the high-frequency regime for $Ni_{79}Fe_{21}$ and Co films of different thickness range from 0.12–0.47 ps. The theoretically calculated values for Fe, Co, and Ni using the Wannier implementation for η ranging from 5–10 meV are reported in Table I and lie roughly in the above-mentioned experimental range for the ferromagnetic films.

V. CONCLUSIONS

In summary, in this paper we have presented a numerical method to obtain the Gilbert damping and moment of inertia based on the torque-torque correlation model within an *ab initio* Wannier framework. We have also described a technique to calculate the spin-orbit coupling matrix elements via the transformation between the spin-orbit and spin-polarized basis. The damping and inertia calculated using this method for the transition metals like Fe, Co, and Ni are in good agreement with the previous studies based on the tight-binding method [29,30] and local spin density approximation [32]. We have calculated the Bloch relaxation time for the approximate physical range of broadening caused by electron-phonon coupling and lattice defects. The Bloch relaxation time is in good agreement with experimentally reported values using FMR [27]. The calculated damping and moment of inertia can be used to study the magnetization dynamics in the sub-ps regime.

ACKNOWLEDGMENTS

This work has been supported by a financial grant through the Indo-Korea Science and Technology Center (IKST). We thank the Supercomputer Education and Research Centre (SERC) at the Indian Institute of Science (IISc) and the Korea Institute of Science and Technology (KIST) for providing the computational facilities. R.B. acknowledges the funding from the Prime Minister's Research Fellowship (PMRF), MHRD. M.J. and H.R.K. gratefully acknowledge the National Supercomputing Mission of the Department of Science and Technology, India, and the Science and Engineering Research Board of the Department of Science and Technology, India, for financial support under Grants No. DST/NSM/R&D HPC Applications/2021/23 and No. SB/DF/005/2017, respectively. M.J. also acknowledges financial support from Nano Mission of the Department of Science and Technology under Grant No. DST/NM/TUE/QM-10/2019.

[1] M. Fähnle, R. Drautz, R. Singer, D. Steiauf, and D. Berkov, A fast *ab initio* approach to the simulation of spin dynamics, Comput. Mater. Sci. **32**, 118 (2005).

[2] V. P. Antropov, M. I. Katsnelson, M. van Schilfgaarde, and B. N. Harmon, *Ab initio* spin dynamics in magnets, Phys. Rev. Lett. **75**, 729 (1995).

[3] B. Skubic, J. Hellsvik, L. Nordström, and O. Eriksson, A method for atomistic spin dynamics simulations: Implementation and examples, J. Phys.: Condens. Matter **20**, 315203 (2008).

[4] V. P. Antropov, M. I. Katsnelson, B. N. Harmon, M. van Schilfgaarde, and D. Kusnezov, Spin dynamics in magnets: Equation of motion and finite temperature effects, Phys. Rev. B **54**, 1019 (1996).

[5] D. Steiauf and M. Fähnle, Damping of spin dynamics in nanostructures: An *ab initio* study, Phys. Rev. B **72**, 064450 (2005).

[6] S. Parkin, X. Jiang, C. Kaiser, A. Panchula, K. Roche, and M. Samant, Magnetically engineered spintronic sensors and memory, Proc. IEEE **91**, 661 (2003).

[7] Y. Xu and S. Thompson, *Spintronic Materials and Technology* (CRC Press, Boca Raton, FL, 2006).

[8] K.-W. Kim and H.-W. Lee, Chiral damping, Nat. Mater. **15**, 253 (2016).

[9] A. V. Chumak, V. I. Vasyuchka, A. A. Serga, and B. Hillebrands, Magnon spintronics, Nat. Phys. **11**, 453 (2015).

[10] T. L. Gilbert, A phenomenological theory of damping in ferromagnetic materials, IEEE Trans. Magn. **40**, 3443 (2004).

[11] S. Bhattacharjee, L. Nordström, and J. Fransson, Atomistic spin dynamic method with both damping and moment of inertia effects included from first principles, Phys. Rev. Lett. **108**, 057204 (2012).

[12] M.-C. Ciornei, J. M. Rubí, and J.-E. Wegrowe, Magnetization dynamics in the inertial regime: Nutation predicted at short time scales, Phys. Rev. B **83**, 020410(R) (2011).

[13] D. Böttcher and J. Henk, Significance of nutation in magnetization dynamics of nanostructures, Phys. Rev. B **86**, 020404(R) (2012).

[14] R. Wieser, Comparison of quantum and classical relaxation in spin dynamics, Phys. Rev. Lett. **110**, 147201 (2013).

[15] A. Chudnovskiy, C. Hübner, B. Baxevanis, and D. Pfannkuche, Spin switching: From quantum to quasiclassical approach, Phys. Status Solidi B **251**, 1764 (2014).

[16] G. D. Fuchs, J. C. Sankey, V. S. Pribiag, L. Qian, P. M. Braganca, A. G. F. Garcia, E. M. Ryan, Z.-P. Li, O. Ozatay, D. C. Ralph, and R. A. Buhrman, Spin-torque ferromagnetic resonance measurements of damping in nanomagnets, Appl. Phys. Lett. **91**, 062507 (2007).

[17] M. Oogane, T. Wakitani, S. Yakata, R. Yilgin, Y. Ando, A. Sakuma, and T. Miyazaki, Magnetic damping in ferromagnetic thin films, Jpn. J. Appl. Phys. **45**, 3889 (2006).

[18] E. Barati, M. Cinal, D. Edwards, and A. Umerski, Calculation of Gilbert damping in ferromagnetic films, in *EPJ Web of Conferences*, Vol. 40 (EDP Sciences, Les Ulis, France, 2013), p. 18003.

[19] S. Bhagat and P. Lubitz, Temperature variation of ferromagnetic relaxation in the *3d* transition metals, Phys. Rev. B **10**, 179 (1974).

[20] F. Schreiber, J. Pflaum, Z. Frait, T. Mühge, and J. Pelzl, Gilbert damping and g-factor in Fe_xCo_{1-x} alloy films, Solid State Commun. **93**, 965 (1995).

[21] N. Inaba, H. Asanuma, S. Igarashi, S. Mori, F. Kirino, K. Koike, and H. Morita, Damping constants of Ni-Fe and Ni-Co alloy thin films, IEEE Trans. Magn. **42**, 2372 (2006).

[22] H.-S. Song, K.-D. Lee, J.-W. Sohn, S.-H. Yang, S. S. Parkin, C.-Y. You, and S.-C. Shin, Observation of the intrinsic Gilbert damping constant in Co/Ni multilayers independent of the stack number with perpendicular anisotropy, Appl. Phys. Lett. **102**, 102401 (2013).

[23] S. Mizukami, E. Sajitha, D. Watanabe, F. Wu, T. Miyazaki, H. Naganuma, M. Oogane, and Y. Ando, Gilbert damping in perpendicularly magnetized Pt/Co/Pt films investigated by all-optical pump-probe technique, Appl. Phys. Lett. **96**, 152502 (2010).

[24] A. Trunova, Ferromagnetische resonanz an oxidfreien magnetischen Fe und FeRh nanopartikeln, Ph.D. thesis, Vom Fachbereich Physik der Universität Duisburg-Essen, Essen, Germany, 2009.

[25] B. Heinrich and Z. Frait, Temperature dependence of the FMR linewidth of iron single-crystal platelets, Phys. Status Solidi B **16**, K11 (1966).

[26] Y. Zhao, Q. Song, S.-H. Yang, T. Su, W. Yuan, S. S. P. Parkin, J. Shi, and W. Han, Experimental investigation of temperature-dependent Gilbert damping in permalloy thin films, Sci. Rep. **6**, 22890 (2016).

[27] Y. Li, A.-L. Barra, S. Auffret, U. Ebels, and W. E. Bailey, Inertial terms to magnetization dynamics in ferromagnetic thin films, Phys. Rev. B **92**, 140413(R) (2015).

[28] N. Umetsu, D. Miura, and A. Sakuma, Theoretical study on Gilbert damping of nonuniform magnetization precession in ferromagnetic metals, J. Phys. Soc. Jpn. **81**, 114716 (2012).

[29] D. Thonig and J. Henk, Gilbert damping tensor within the breathing Fermi surface model: Anisotropy and non-locality, New J. Phys. **16**, 013032 (2014).

[30] D. Thonig, O. Eriksson, and M. Pereiro, Magnetic moment of inertia within the torque-torque correlation model, Sci. Rep. **7**, 931 (2017).

[31] D. Thonig, Y. Kvashnin, O. Eriksson, and M. Pereiro, Nonlocal Gilbert damping tensor within the torque-torque correlation model, Phys. Rev. Mater. **2**, 013801 (2018).

[32] K. Gilmore, Y. U. Idzerda, and M. D. Stiles, Identification of the dominant precession-damping mechanism in Fe, Co, and Ni by first-principles calculations, Phys. Rev. Lett. **99**, 027204 (2007).

[33] H. Ebert, S. Mankovsky, D. Ködderitzsch, and P. J. Kelly, *Ab initio* calculation of the Gilbert damping parameter via the linear response formalism, Phys. Rev. Lett. **107**, 066603 (2011).

[34] K. Gilmore and M. D. Stiles, Evaluating the locality of intrinsic precession damping in transition metals, Phys. Rev. B **79**, 132407 (2009).

[35] V. Kamberský, Spin-orbital Gilbert damping in common magnetic metals, Phys. Rev. B **76**, 134416 (2007).

[36] J. Kuneš and V. Kamberský, First-principles investigation of the damping of fast magnetization precession in ferromagnetic 3d metals, Phys. Rev. B **65**, 212411 (2002).

[37] V. Kamberský, FMR linewidth and disorder in metals, Czech. J. Phys. B **34**, 1111 (1984).

[38] V. Kamberský, On the Landau–Lifshitz relaxation in ferromagnetic metals, Can. J. Phys. **48**, 2906 (1970).

[39] V. Kamberský, On ferromagnetic resonance damping in metals, Czech. J. Phys. B **26**, 1366 (1976).

[40] L. F. Mattheiss and D. R. Hamann, Linear augmented-plane-wave calculation of the structural properties of bulk Cr, Mo, and W, Phys. Rev. B **33**, 823 (1986).

[41] D. Papaconstantopoulos and M. J. Mehl, The Slater-Koster tight-binding method: A computationally efficient and accurate approach, J. Phys.: Condens. Matter **15**, R413 (2003).

[42] N. Marzari, A. A. Mostofi, J. R. Yates, I. Souza, and D. Vanderbilt, Maximally localized Wannier functions: Theory and applications, Rev. Mod. Phys. **84**, 1419 (2012).

[43] G. Pizzi, V. Vitale, R. Arita, S. Blügel, F. Freimuth, G. Géranton, M. Gibertini, D. Gresch, C. Johnson, T. Koretsune *et al.*, Wannier90 as a community code: New features and applications, J. Phys.: Condens. Matter **32**, 165902 (2020).

[44] I. Souza, N. Marzari, and D. Vanderbilt, Maximally localized Wannier functions for entangled energy bands, Phys. Rev. B **65**, 035109 (2001).

[45] S. Roychoudhury and S. Sanvito, Spin-orbit Hamiltonian for organic crystals from first-principles electronic structure and Wannier functions, Phys. Rev. B **95**, 085126 (2017).

[46] F. Mahfouzi, J. Kim, and N. Kioussis, Intrinsic damping phenomena from quantum to classical magnets: An *ab initio* study of Gilbert damping in a Pt/Co bilayer, Phys. Rev. B **96**, 214421 (2017).

[47] A. Kamra, R. E. Troncoso, W. Belzig, and A. Brataas, Gilbert damping phenomenology for two-sublattice magnets, Phys. Rev. B **98**, 184402 (2018).

[48] A. Brataas, Y. Tserkovnyak, and G. E. W. Bauer, Scattering theory of Gilbert damping, Phys. Rev. Lett. **101**, 037207 (2008).

[49] P. Giannozzi, S. Baroni, N. Bonini, M. Calandra, R. Car, C. Cavazzoni, D. Ceresoli, G. L. Chiarotti, M. Cococcioni, I. Dabo *et al.*, Quantum Espresso: A modular and open-source software project for quantum simulations of materials, J. Phys.: Condens. Matter **21**, 395502 (2009).

[50] P. Giannozzi, O. Andreussi, T. Brumme, O. Bunau, M. B. Nardelli, M. Calandra, R. Car, C. Cavazzoni, D. Ceresoli, M. Cococcioni *et al.*, Advanced capabilities for materials modelling with quantum espresso, J. Phys.: Condens. Matter **29**, 465901 (2017).

[51] A. I. Liechtenstein, M. Katsnelson, V. Antropov, and V. Gubanov, Local spin density functional approach to the theory of exchange interactions in ferromagnetic metals and alloys, J. Magn. Magn. Mater. **67**, 65 (1987).

[52] M. Fähnle, D. Steiauf, and C. Illg, Erratum: Generalized Gilbert equation including inertial damping: Derivation from an extended breathing Fermi surface model [Phys. Rev. B **84**, 172403 (2011)], Phys. Rev. B **88**, 219905(E) (2013).